

A Finite Element Formulation for Atrial Tissue Monolayer

L. Wieser¹, H. E. Richter¹, G. Plank², B. Pfeifer¹, B. Tilg¹, C. N. Nowak¹, G. Fischer¹

¹Institute of Biomedical Engineering, University for Health Sciences, Medical Informatics and Technology (UMIT), Hall i. T., Austria

²Institute for Biophysics, Graz Medical University, Graz, Austria

Summary

Objectives: Using computer models for the study of complex atrial arrhythmias such as atrial fibrillation is computationally demanding as long observation periods in the order of tens of seconds are required. A well established approach for reducing computational workload is to approximate the thin atrial walls by curved monolayers. On the other hand, the finite element method (FEM) is a well established approach to solve the underlying partial differential equations.

Methods: A generalized 2D finite element method (FEM) is presented which computes the corresponding stiffness and coupling matrix for arbitrarily shaped monolayers (ML). Compared to standard 2D FEM, only one additional coordinate transformation is required. This allows the use of existing FEM software with minor modifications. The algorithm was tested to simulate wave propagation in benchmark geometries and in a model of atrial anatomy.

Results: The ML model was able to simulate electric activation in curved tissue with anisotropic conductivity. Simulations in branching tissue yielded slightly different patterns when compared to a volumetric model with finite thickness. In the model of atrial anatomy the computed activation times for five different pacing protocols displayed a correlation of 0.88 compared to clinical data.

Conclusions: The presented method provides a useful and easily implemented approach to model wave propagation in MLs with a few restrictions to volumetric models.

Keywords

Computer model, monolayer, finite element method, atria

Methods Inf Med 2008; 47: 131–139

doi:10.3414/ME0414

1. Introduction

Atrial fibrillation (AF) is the most common supraventricular arrhythmia with a prevalence rising from 0.5% of people in their 50s to nearly 10% of people over 80 [1, 2]. AF causes remodeling of the atrial tissue which in turn favors the development of chronic AF [3-5]. Despite its importance, the mechanisms underlying the formation of AF and how AF is sustained long enough to lead to a chronic disease remains poorly understood.

Complementary to experimental techniques, computer models of atrial activation [6, 7] are among the most elegant research tools to gain insight into underlying mechanisms. Several details can be included, ranging from cellular level (e.g. ionic channels) to tissue level [8]. However, due to the nature of AF, long observation periods are required which make simulation studies computationally demanding. In [9], a full three-dimensional (3D) anatomically realistic atrial model based on the finite volume method has been presented. Simulations could reproduce experimentally observed activation patterns during sinus rhythm and single site pacing. Although supercomputing facilities were used to run simulations, due to the tremendous computational workload imposed by a full 3D model (volumetric mesh grid throughout the atrial wall) simulations were limited to about 100 ms of activity. In [6], a morphologically realistic atrial model, built upon three-dimensionally curved layers of interconnected cables [10], has been used to simulate reentrant activity of about 1 s. The computationally very efficient cable approach lends itself easily to a parallel implementation since each cable

first can be considered as isolated. In a subsequent step, current flow between the cables is taken into account by using functions which satisfy the homogeneous solution. As shown in [11], a further reduction in computational demand can be achieved by approximating the relatively thin atrial wall by a shell or monolayer (ML) curved in the three-dimensional space. A finite volume scheme was employed in [7] to simulate 40 s of AF in an anatomically realistic ML mesh of the human atria.

In this paper a FEM-based ML method is presented: 1) As in [11], using a ML approximation results in a significantly smaller number of unknowns thus reducing computational demands. 2) Unlike FEM, none of the above mentioned methods are based on error minimization nor can they handle complex geometries and spatial heterogeneities as straightforwardly as the FEM does. 3) The considerably greater body of mathematics and error analysis around the FEM method led to numerous implementations. The FEM-ML method can be based upon existing FEM codes with minor modification. Only a single additional coordinate transformation is required, all other parts of existing FEM codes (computation of the element matrices, assembly of global matrices) remain unaffected.

In this article, a conventional two-dimensional (2D) FEM technique using linear triangular elements is generalized to a 3D ML technique which is applicable to arbitrary shapes including branching structures. A code example written in the MATLAB® (The MathWorks, Inc.) language is given. Finally, the method is applied to compute wave propagation in various benchmark models: In simple geometries the results ob-

tained by the FEM-ML technique are compared to results in corresponding volumetric models in order to study possible restrictions of the ML approximation. Also, a model of human atria (ML representation) was constructed, and simulations for single site pacing were compared to previous atrial models and to a clinical study.

2. Methods

We aim to describe the propagation of electric activation in atrial tissue and make use of the monodomain equation. This is a simplification of the more accurate and computationally more expensive bidomain equations [10]. Nevertheless, it has been shown to be an adequate approximation if only wave propagation in cardiac tissue has to be modeled [12]. The monodomain equation is a reaction-diffusion type equation, i.e. excited cells give depolarizing charge to their neighboring cells to spread the excitation.

2.1 Monolayer Finite Element Method

We assume cardiac tissue as a 3D monolayer (domain A), on which we describe wave-front propagation by the continuous monodomain equation

$$\frac{1}{\beta} \operatorname{div}(\boldsymbol{\sigma} \operatorname{grad} V(\vec{r}, t)) = C_m \frac{\partial V(\vec{r}, t)}{\partial t} + J_{\text{ion}}(\vec{r}, t) \quad (1)$$

and a non-flux boundary condition. Here, $V(\vec{r}, t)$ is the transmembrane potential, β is the surface to volume ratio of the cell, C_m is the cell capacitance per unit area, $J_{\text{ion}}(\vec{r}, t)$ is the ionic current density provided by the ionic current model, and $\boldsymbol{\sigma}$ is the conductivity tensor which is determined by a longitudinal and a transversal conductivity (σ_{\parallel} and σ_{\perp} , respectively) and a fiber direction. We denote tensors by bold letters and vectors by arrows. First of all, the spatial discretization requires a division of the domain into triangles as finite elements.

Ideally, the edge lengths of the triangles have only little variation. In [13], a systematic under-estimation of the simulated conduction velocity is reported, depending on the distance between the computational nodes. Therefore, in a mesh with large variation of the inter-nodal distance (edge length) also the conduction velocity error would vary throughout the mesh. Elements may have a common edge with more than one other element simultaneously. By this means, branching structures can be included into the model. Furthermore, a fiber direction (unit vector, contained in the triangle plane) and conductivities are assigned to each element. The element functions n_i are piecewise linear and take values δ_{ij} on each node j . Consequently, all spatially distributed functions can be written as linear combination of the n_i

$$V(\vec{r}, t) = V = \sum_i V_i n_i$$

$$J_{\text{ion}}(\vec{r}, t) = J_{\text{ion}} = \sum_i J_i n_i \quad (2)$$

Applying the FEM (Ritz-approach), we write the coefficient vectors of V and J_{ion} as \tilde{V} and \tilde{J} respectively, and we obtain the space discretized form of (1):

$$-\mathbf{S}\tilde{V} = \beta \mathbf{T} \left(C_m \frac{\partial \tilde{V}}{\partial t} + \tilde{J} \right) \quad (3)$$

The matrices of interest, the stiffness matrix \mathbf{S} and the coupling matrix \mathbf{T} are then defined by

$$\mathbf{S}_{ij} = \int_A \operatorname{grad} n_i (\boldsymbol{\sigma} \operatorname{grad} n_j) dA \quad (4)$$

$$\mathbf{T}_{ij} = \int_A n_i n_j \delta A, \quad (5)$$

where gradients in (4) are in a 2D sense, i.e. derivatives into two orthogonal directions on the tangent plane.

For a domain A entirely in the 2D space a standard FEM algorithm determines \mathbf{S} and \mathbf{T} in a loop over each element E_k , and the single element matrices

$$\mathbf{s} = \int_{E_k} \operatorname{grad} n_i (\boldsymbol{\sigma} \operatorname{grad} n_j) dA \quad (6)$$

$$\mathbf{t} = \int_{E_k} n_i n_j dA \quad (7)$$

are assembled to the global matrices. In the case of monolayers the elements can be located arbitrarily in 3D space. Thus, before the element matrix calculation an additional transformation has to be performed, which carries each element into a new x^*-y^* -coordinate system. This transformation should conserve shape and size of the triangles and eliminate the z -component of their vertices. Denoting the vertices of the original triangle E_k by \vec{p}_1^* , \vec{p}_2^* and \vec{p}_3^* , the new coordinates (*) can be written

$$\vec{p}_1^* = \begin{pmatrix} 0 \\ 0 \end{pmatrix}, \quad \vec{p}_2^* = \begin{pmatrix} |\overrightarrow{p_1 p_2}| \\ 0 \end{pmatrix},$$

$$\vec{p}_3^* = \begin{pmatrix} |\overrightarrow{p_1 p_3}| \cos(\Phi) \\ |\overrightarrow{p_1 p_3}| \sin(\Phi) \end{pmatrix} \quad (8)$$

where Φ is the angle between $\overrightarrow{p_1 p_2}$ and $\overrightarrow{p_1 p_3}$, ranging from 0 to π . Analogously, the fiber direction \vec{f} is transformed into the vector \vec{f}^* such, that its relative position in the triangle does not change. The conductivity tensor in (*)-coordinates is then

$$\boldsymbol{\sigma}^* = \begin{pmatrix} f_x^* & -f_y^* \\ f_y^* & f_x^* \end{pmatrix} \begin{pmatrix} \sigma_{\parallel} & 0 \\ 0 & \sigma_{\perp} \end{pmatrix} \begin{pmatrix} f_x^* & f_y^* \\ -f_y^* & f_x^* \end{pmatrix} \quad (9)$$

At this point, a standard 2D FEM routine for element matrix calculation and assembling can be applied to E_k^* and $\boldsymbol{\sigma}^*$. The entire procedure can be summarized as follows:

- For each element E_k
- 1) perform an isometric transformation into the virtual x^*-y^* -plane, obtaining E_k^* ,
- 2) apply the same transformation to the fiber vector \vec{f} , obtaining \vec{f}^* and $\boldsymbol{\sigma}^*$,
- 3) use a 2D FEM standard routine to get the corresponding element matrices \mathbf{s} and \mathbf{t} , and
- 4) assemble \mathbf{s} and \mathbf{t} to the global stiffness and coupling matrix.

Note that the only differences to a standard 2D FEM algorithm are points 1 and 2, where an additional coordinate transformation is applied.

2.2 Code Example

In this section a MATLAB code example is given using the command *assema* which is contained in *PDEtool*, a toolbox for partial differential equations. Analogously, any other 2D FEM software can be extended to ML formulation.

The entire body of the algorithm is shown in Figure 1, the additional coordinate transformation is shown separately in Figure 2. Both files can be downloaded from <http://bm.umit.at/download.htm>. The routine is divided into four parts according to the four steps in Section 2.1. The MATLAB command $[S,T]=assema(p,t,c,a,f)$ calculates the stiffness (S) and coupling matrix (T) of the elliptic equation

$$\text{div}(\mathbf{c}\text{grad}u) + au = f \quad (10)$$

using the grid stored in p (nodes) and t (triangles). The matrices are equivalent to those of (1), if the parameters in (10) are set to $a = 1$ and $f = 0$. Since we compute the matrices for a single element, the grid which is given to the function consists of 1 triangle: Variable p holds the coordinates of the three nodes (2D), and t contains triangle information (column-wise, one column in our case) where rows 1-3 are used for node numbers and row 4 contains the assigned compartment. Conductivities \mathbf{c} for each element are given as a 2×2 tensor but its four entries have to be aligned in columns (one column in our case).

2.3 Application to Benchmark Models

For validation the algorithm was applied to different benchmark models (comparison ML vs. volumetric geometries), and to a model of the human atria. For the ML models the necessary matrices (stiffness and coupling matrix) were determined using the algorithm presented in Section 2.1. In the case of volumetric models the respective matrices were calculated using a standard 3D FEM scheme with linear tetrahedral elements [14].

```
% matrix definitions
MtS = sparse(nnod,nnod);
MtT = sparse(nnod,nnod);
for elem=1:nelem
    % 1) transform nodes and fibre direction
    v12 = cor(con(elem,2),:)-cor(con(elem,1),:);
    v13 = cor(con(elem,3),:)-cor(con(elem,1),:);
    [cor_st, fib_st] = trans(v12,v13,fib(elem,:));

    % 2) conductivity tensor
    fib_mat = [fib_st(1) -fib_st(2);
              fib_st(2) fib_st(1)];
    sigma_diag = [cond(elem,1) 0;
                 0 cond(elem,2)];
    sigma = fib_mat*sigma_diag*fib_mat';

    % 3) element matrix
    [S,T] = assema(cor_st,[1 2 3 1]',
                  [sigma(:,1); sigma(:,2)],1,0);

    % 4) assembling
    MtS(con(elem,:),con(elem,:)) =
        MtS(con(elem,:),con(elem,:))+S;
    MtT(con(elem,:),con(elem,:)) =
        MtT(con(elem,:),con(elem,:))+T;

end
```

Fig. 1 MATLAB code for matrix generation, four input arguments: *cor* (row-wise 3D coordinates of nodes), *con* (row-wise node numbers belonging to elements), *fib* (row-wise unit vectors of fiber direction of corresponding element), *cond* (row-wise longitudinal and transverse component of conductivity for each element). Denoting the number of nodes by *nnod* and the number of elements by *nelem* we first define sparse stiffness and coupling matrix *MtS* and *MtT*, then the loop over all elements is executed.

2.3.1 Simulation Parameters

Underlying membrane kinetics were described by the Ramirez-Nattel-Courtemanche model [15], making use of lookup tables, whenever possible, in order to accelerate computation. The remaining parameters of (1) were set $C_m = 0.01 \mu\text{F}/\text{mm}^2$ and $\beta = 100/\text{mm}$.

For time discretization an explicit (forward) time scheme with a constant time step $\Delta t = 15 \mu\text{s}$ was used. Applied to Equation 3 this leads to the completely discretized version of the monodomain equation:

$$\mathbf{T}\tilde{V}_{i+1} = \left(-\frac{\Delta t}{\beta C_m} \mathbf{S} + \mathbf{T} \right) \tilde{V}_i - \frac{\Delta t}{C_m} \mathbf{T}\tilde{J} \quad (11)$$

Here, \tilde{V}_i and \tilde{V}_{i+1} are the representations of $V(\vec{r}, t)$ and $V(\vec{r}, t + \Delta t)$ respectively. As in [10], a lumped mass approximation was used to make matrix \mathbf{T} diagonal and the linear system trivial to solve. The algorithm for calculating wave propagation (including the ionic current model) was implemented in C++ and executed on a single Pentium IV processor with 3.2 GHz.

2.3.2 Benchmark Model – Sphere

To study propagation in a uniformly curved test model, a simplified representation of the right atrium was constructed (half sphere of 20 mm diameter with a hole of 2.6 mm diameter on its top, Fig. 3). The orifices may represent caval vein (superior)

```

function [cor_st, fib_st] =
trans(p1p2,p1p3,fib)
% 1st node (zero point)
cor_st(:,1) = [0; 0];
% 2nd node
cor_st(:,2) = [norm(p1p2); 0];
% 3rd node
cosphi = p1p2*p1p3'/(norm(p1p2)*norm(p1p3));
cor_st(:,3) = norm(p1p3)*
    [cosphi;sqrt(1-cosphi^2)];

% orthogonal basis for (p1p2, p1p3)
bas1 = p1p2;
bas2 = p1p3 - (p1p2*p1p3'/norm(p1p2)^2)*p1p2;
% relative coordinates (*-coordinates)
fib_st(1) = fib*bas1'/norm(bas1);
fib_st(2) = fib*bas2'/norm(bas2);
% normalized

fib_st = fib_st/norm(fib_st);

```

Fig. 2 This function transforms a triangular element (given by vectors $\overrightarrow{p_1p_2}$ and $\overrightarrow{p_1p_3}$ and the corresponding fiber vector \vec{f} into (*)-coordinates.

and tricuspid annulus (bottom). We provided the model with anisotropic conductivity by including fibers between the longitudes 0° and 12° , running from top to the base. This detail was chosen according to a faster conductivity along the crista terminalis [16, 17]. In the fibrous region the conductivities were $\sigma_{\parallel} = 0.3$ S/m and $\sigma_{\perp} = 0.1$ S/m, whereas on the rest of the surface we assigned an isotropic conductivity of $\sigma = 0.1$ S/m. A stimulus was applied at the top edge of the fibrous region (presumed sinus node). For validation, the same stimulus was applied to a corresponding volumetric model (constant wall thickness of 2 mm, equivalent conductivities and fibers as the ML model). The results (activation times and local conduction velocities) obtained for the ML model and the mid-layer of the volumetric model were then compared.

2.3.3 Benchmark Model – Branching Tissue

Particular focus was set on branching tissue, a structure that can be frequently found in the atria. Bundles branching off from cardiac tissue can affect propagating waves as

they constitute additional load for the depolarizing current [18]. In ML formulation, such bundles can be represented by strip-like bands connected to the remaining tissue. However, due to the 2D nature of monolayers, bundle insertions have no finite thickness in contrast to a corresponding 3D representation. Thus, the additional electric load provided by the bundle appears too abrupt for propagating waves. In order to study this phenomenon, a benchmark model was constructed, which consisted of a rectangular tissue with a single bundle (represented as a 3.2 mm strip) branching off from its center. The activation pattern initiated by single site pacing in this model was compared to a corresponding 3D model with 2 mm thickness and a bundle of cylindrical shape and a diameter of 3.2 mm (see Fig. 5a). In both, the 2D- and 3D-model, the tissue conductivity was isotropic (0.1 S/m), whereas in the bundle the longitudinal component was three times higher (0.3 S/m) than the transversal, in order to account for the longitudinal fibers.

2.3.4 Atrial Model

Furthermore, a ML model of the atrial geometry was constructed based on magnetic resonance imaging (MRI) data of a 25-year-old female patient with a supraventricular tachycardia and a structurally normal heart. After segmentation of the atria (details can be found in [19, 20]), a gross ML representation of the atria was available. The MRI-based model contained the mitral and tricuspid annulus, the ostia of superior and inferior vena cava (SVC, IVC), the pulmonary veins (PV), and the left and right atrial appendages (LAA, RAA). For obtaining a high-quality mesh (little variation in edge length, see Section 2.1) the data were exported to a commercial mesh generator (HyperMesh, Altair Engineering, Troy, MI) by subdividing the atria into 231 spline surfaces (145 right, 86 left). The geometry was remeshed with a mean edge length of $200 \mu\text{m}$. Anatomical structures which could not be identified from the MRI data, i.e. the crista terminalis (CT), the coronary sinus (CS), Bachmann's bundle (BB) and the fossa ovalis (FO), were incorporated manually according to data presented in [9, 21]. Thus, the model contained the three main conductive structures between left and right atrium, as reported by [22]. Note, that BB and the CS are branching structures in the sense of the model in the previous paragraph. As in [9], the sinus node (SN) was located at the superior end of the CT (Fig. 6). Both atria were provided with isotropic conductivities (0.12 S/m) except in bundles (CT, CS and BB) where longitudinal conductivity (0.72 S/m) was six times higher than the transversal one. These values were chosen based on the model of Seemann et al. [23] and resulted in conduction velocities of about 50 cm/s in isotropic tissue and about 130 cm/s along the bundles (60 cm/s resp. 110–160 cm/s in [23]). Additionally, the conductivity around the fossa ovalis was set to 0.03 S/m (leading to a conduction velocity of about 25 cm/s, similar as in [9]). Single site pacing was performed at different locations, including the SN, the anterolateral high right atrium, the CS ostium, and the right insertion of BB, in order to compare the simulation results to a previous clinical study [24].

3. Results

3.1 Sphere

The isochrones of activation for the volumetric mesh and ML model are shown in Figure 3. After stimulation, the wavefront spreads out into all possible directions. Preferred propagation along the given fibers can be recognized by the convex curvature of the isochrones (left panel). After encircling the superior orifice from both directions, the wavefronts collide opposite the stimulus site and propagate from superior to the base. Activation times in the ML and volumetric mesh formulation are similar, and their root mean square difference is 0.2 ms (range -0.4 ms to 0.6 ms), at a total activation time of 47 ms.

Figure 4 shows the distribution of conduction velocity in the ML (solid lines) and volumetric mesh formulation (dashed lines) along longitudes in the fibrous region and at the opposite side. Again, good coincidence is observed. The velocity of wavefront propagation starts at a value of about 0.5 m/s and increases continuously. As can be seen in Figure 3 the wavefront has a convex curvature in the fibrous region. Thus, it does not reach the velocity of a plane wave propagating in tissue with the same conductivity (dotted, horizontal line). The final rise of the conduction up to 2.4 m/s is due to the collision with the border of the tissue. On the opposite side the two wavefronts collide at the superior edge (latitude 15°) forming a wavefront with a concave curvature. Thus, the conduction velocity is higher than the corresponding value of 1D propagation. With decreasing curvature also the conduction velocity decreases. Finally, conduction velocity at the border rises to about 0.85 m/s (decreased load).

3.2 Branching Tissue

The wavefront is influenced by the bundle insertion in both the volumetric and the ML model. Figure 5 shows action potential upstrokes at different points along a line in propagation direction. The location and the shape of the bundle are outlined for each model. When the wavefront reaches the

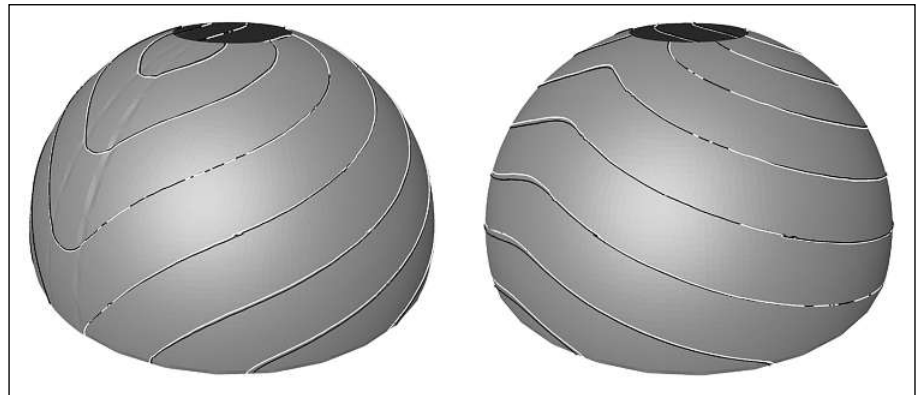


Fig. 3 Front view (left) and back view (right) of the sphere. Activation times in the monolayer formulation are depicted by white isolines, ranging from 0 ms to 45 ms in 5 ms steps. The black lines show the corresponding activation times in the middle layer of the volumetric mesh model.

edge of the cylindrical bundle (Fig. 5B, first bold AP), depolarizing current is drawn from the tissue (additional load), resulting in a reduced upstroke and a delayed propagation (pull effect). Propagation through the bundle insertion continues in a rather unaffected manner, but at the opposite edge of the bundle a reverse effect is observed (Fig. 5B, second bold AP): The bundle now injects current back into the tissue and increases depolarization (push effect). Thus, propagation is slightly accelerated at this

point. A similar behavior is observed for the ML model (Fig. 5C), although in this case the bundle constitutes a more abrupt obstacle without finite thickness: Now, the push effect is recognized immediately after the appearance of the pull effect, when the wavefront reaches the branch point. Furthermore, both effects are more pronounced. The effective propagation delay caused by the bundle was measured in the ML and the volumetric model for various diastolic intervals. For long diastolic inter-

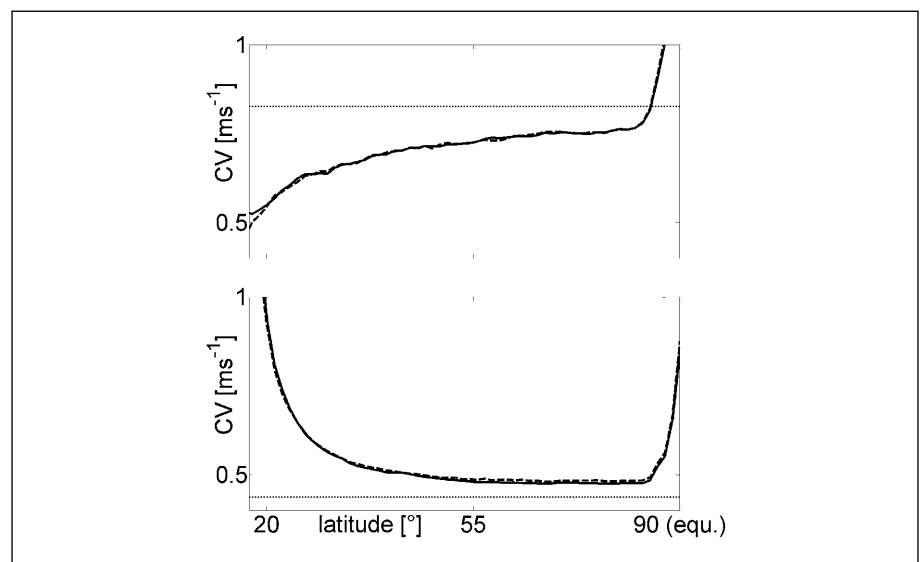


Fig. 4 Conduction velocity distribution in the ML (solid) and the volumetric (dashed) model along two longitudes: middle line of the fibrous region (at 6° , upper panel), opposite line (at 186° , lower panel). The dotted horizontal lines indicate the velocities of a plane wavefront at the longitudinal conductivity of the fibers (upper panel) and at the conductivity of the bulk tissue (lower panel).

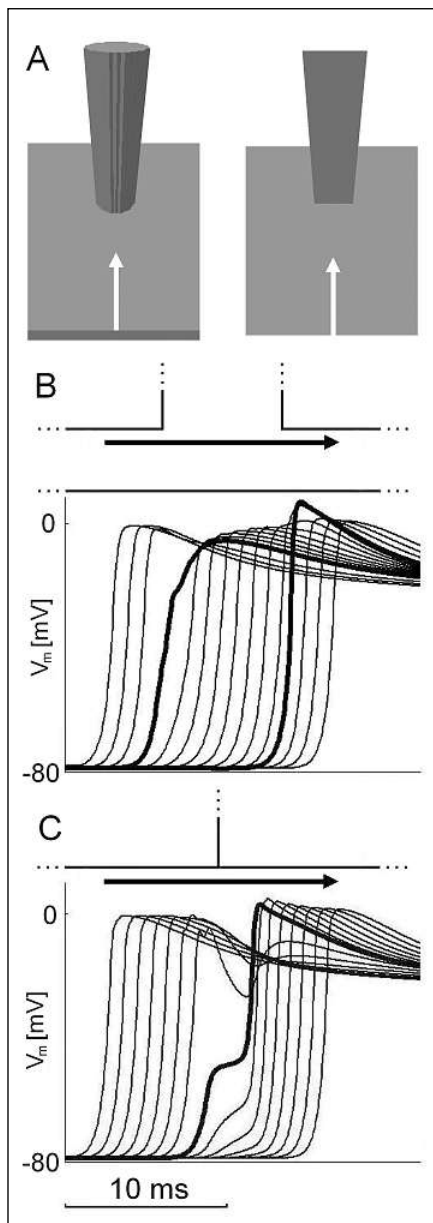


Fig. 5 Panel A shows the bundle geometries for the volumetric and the ML representation, together with the propagation direction of the wavefront (white arrows). Action potential (AP) upstrokes are displayed for the volumetric (B) and the ML model (C) in 4 mm steps in propagation direction. The profile of the bundle in each model is indicated above the respective AP plot (with an arrow pointing into the propagation direction), and its edges are marked by bold lines for the APs.

vals (200 ms and more) the travel time of the wavefront across the bundle (distance 3.2 mm) was about 1 ms longer in the ML case than for the volumetric model. This value increased to about 1.4 ms for the shortest possible diastolic interval.

3.3 Atrial Model

The simulation of 1 s of cardiac activity in the atrial model (162,734 computational nodes) takes 344 min of CPU time on a single 3.2 GHz Pentium processor with a time step of $\Delta t = 15 \mu\text{s}$. From these, 41 min are needed for the diffusion part of the monodomain equation, the rest is required by the ionic current description.

3.3.1 Sinus Rhythm

The simulated sinus activation sequence is shown in Figure 6 in right anterior and right posterior oblique view. The wavefront spreads out from the sinus node, with fast propagation along the CT. Bachmann's bundle becomes activated after 20 ms, and it is traversed within 10 ms. Thus, the first activation of the left atrium occurs after 30 ms at the left atrial insertion of BB. Subsequently, a wavefront reaches the left atrium via the slow conducting fossa ovalis (31 ms) and collides with the wavefront from BB at 50 ms. Another activation front reaches the connection between left atrium and CS after 59 ms. At this time, the wavefront coming from BB already enters the LAA. The last region excited in the right atrium (at 70 ms) is located at the tricuspid valve (right anterior lateral wall). The last regions excited in the left atrium are the posterior wall (three wavefronts collide near the ostium of the left pulmonary vein) and the outermost left atrial appendix (101 ms). The activation pattern and activation times are in good agreement with the sinus activation in [9] (fully volumetric mesh): The wavefront spreads out from the sinus node in a similar fashion, and activates the left atrium for the first time by Bachmann's bundle (about 30 ms). The activation of the fossa ovalis occurs about 10 ms later than in our model, the coronary sinus is missing in [9]. The right atrium is entirely activated after 100 ms, and the last portion depolarized is the isthmus at the floor of the right atrium. This differs from our result, as a smaller conductivity was assigned to the isthmus in [9]. The last part activated is located in the lateral inferior left atrium (108 ms), similar as in our model.

The activation times were also compared to the values obtained for the simulated

Table 1 Total activation times for different stimulation protocols, correlation coefficient: 0.88

Stimulus site	Model [ms]	Clinical data [ms]
SN	101.1	92
BB	87.9	96
CS ostium	117.4	108
high right atrium	131.9	121
distal CS	123.9	126

sinus rhythm in [23]: The authors report activation times of 83 ms for the RA, 79 ms for the LA and 103 ms for both atria. In the present study these activation times are 70 ms, 71 ms and 101 ms, respectively.

3.3.2 Single Site Stimulation

The model was stimulated at four further locations, according to a previous clinical study protocol [24]. The stimulus sites in the model are indicated in Figure 6 (gray spheres). Total activation times in the simulations and in the clinical study are listed in Table 1. Both the absolute values (mean absolute difference ~ 8 ms) and their relations (correlation coefficient of 0.88) are in good agreement, indicating that the conduction system is well reproduced by the atrial model.

4. Discussion

Computer modeling of cardiac activity is an established investigation tool in cardiac electrophysiology [6, 25, 26]. The ML finite element formulation presented in this study provides a possibility to describe electric wave propagation in thin cardiac tissue, as for example in the atria. Its main advantage is the reduced computational effort compared to volumetric models (e.g. [9, 23]).

4.1 Algorithm

The ML formulation has been used before for computation of wave propagation on atrial tissue [13, 27], and even for detailed

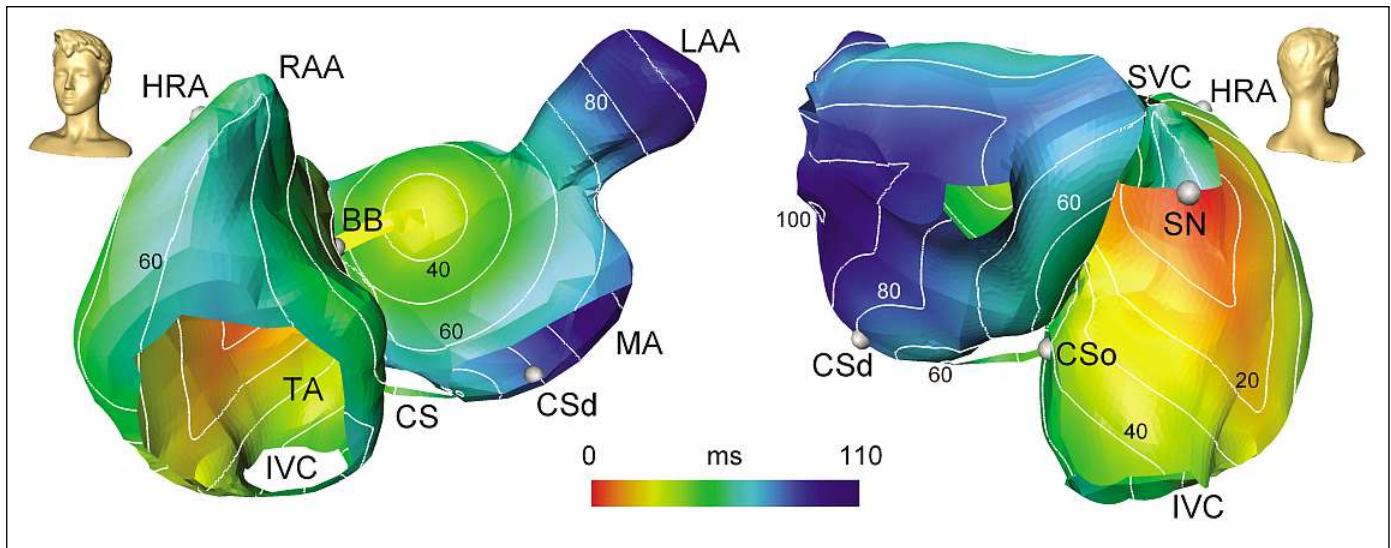


Fig. 6 Activation times in the atrial model in sinus rhythm: The isolines range from 0 ms to 100 ms in 10 ms steps. Beside the sinus node (SN), also other locations were stimulated in this study (marked by the gray spheres): high right atrium (HRA), CS ostium (CSo), distal CS (CSd), and right BB insertion. Other abbreviations are used as in the text. The numbers 20, 40, 60, 80 and 100 identify the corresponding isochrones (in ms).

anatomical models of the atria [7]. In fact, since linear elements on a triangular mesh are also used in [27], the stiffness matrix is the same as in this study, as an analytical consideration shows. When applying lumped mass approximation, coupling matrices also coincide with those in [27]. Nevertheless, the formulation presented here has its particular advantage when generating the global matrices, because it is based on standard FEM 2D algorithms. Such type of software is widely available and can be adapted to the ML formulation by including only one additional coordinate transformation. To give a code example of the algorithm for the generation of the FEM matrices, we chose the MATLAB language which is an interpreted language. This makes the implementation relatively slow since a *for*-loop is used over all elements. Thus, the presented routine is not computation time-optimized and rather should give an illustration of the algorithm.

4.2 Validation

For validation of the FEM ML method, we performed simulations on various test models, including a spherical representation of

the right atrium (uniform curvature). Wave propagation was in good coincidence to a corresponding volumetric model, and differences in activation times did not exceed 0.6 ms (root mean square of 0.2 ms), which means that the effect of the curvature could be accurately reproduced.

The presented ML approach is able to include branching structures, an important feature for atrial tissue (cf. left and right insertion of Bachmann's bundle in the atrial model, Fig. 6), which is believed to give rise to unidirectional block [28], wavefront fractionation and fibrillatory conduction [29, 30]. However, a significant artifact is seen compared to a volumetric representation of tissue: The wavefront (thickness of about 1 mm) immediately undergoes the entire load of the bundle, whereas in the 3D case the load is distributed over a finite thickness. Thus, the pull and push effect are more pronounced in the ML model, and the delay for propagating across the bundle insertion is between 1 ms and 1.4 ms higher.

We also computed wave propagation (single site pacing including sinus activation) in an atrial model, which was a representation of the atria by multiple surfaces curved in space. It is an interesting anatomical feature that the two atria are well separated domains with only a few distinct

inter-atrial connections (a large septum like in the ventricles is missing). Similar to the atrial models described in [9], our model connected the atria by Bachmann's bundle and the fossa ovalis. Here, due to the nature of the monolayer formulation, Bachmann's bundle was a strip-like connection with the properties (overestimation of load effects) described above. The septal connection of both atria was established by the rim of the fossa ovalis. The non-conducting membrane of the fossa was not included in the model as it has a pure hemodynamic but no electrical function. The observation of transseptal conduction in humans needs sophisticated pacing protocols [22], which suggest a delayed conduction across this structure. To account for this we assumed reduced conductivity in the rim.

An additional inter-atrial connection missing in several early computer models [7, 9, 23] is the muscular bridge from the coronary sinus ostium to the posterior basal left atrium [22]. This connection has been modeled by a narrow strip-like structure in a proper anatomical location [31]. The pectinate muscles in the right atrium were not included due to the lack of detailed anatomical data. However, the presented method could cope with a coarse representation of such a structure e.g. by local vari-

ation of conductivity or bundle-like structures.

A first validation of the atrial model was performed by comparing the computed activation intervals for five distinct pacing protocols with clinical data [24]. A correlation coefficient of 0.88 seems reasonable given the large inter-individual variation for atrial activation [32]. Furthermore, for the clinical study the catheters were placed at the pacing location under x-ray fluoroscopy guidance which hampers an exact match with the pacing sites in the computer model. This effect seems to be most pronounced for pacing at BB. In the clinical setting BB is not visible in the x-ray image and the catheter is placed in a position where the right atrial insertion of BB is anatomically expected. In contrast in the computer model pacing is performed at the true insertion of BB resulting in a perfect synchronization of both atria.

Comparing the simulated activation sequence for sinus rhythm with human data several features are qualitatively well reproduced [32] (Fig. 6). At the posterior lateral right atrium a fast cranio-caudal activation is observed due to the effect of the crista terminalis. The first left atrial activation originates from BB. The posterior basal atrium is activated via the CS and the rim of the fossa ovalis.

Any model is per definition a simplified picture of the reality. The degree of simplifications made in a model always depends on the aimed objectives. Here, the use of 3D monolayers enables a relatively fast computation, which is at the cost of a number of limitations: Any type of 3D structures cannot be included directly. It is difficult to simulate the behavior of variable wall thickness or transmural heterogeneities in a pure surface representation. However, the basic mechanism caused by load effects in branching tissue can be principally reproduced in a ML model. The particular strength of a monolayer model is the possibility to simulate long periods of atrial activation due to the relatively small number of nodes in the mesh. This is of particular interest for computer models of atrial fibrillation. This disease can even appear in a chronic form with sustained runs over months. When investigating mechanisms

which maintain the arrhythmia over a long period (mother rotor hypothesis [29]) at least several minutes of atrial fibrillation have to be simulated. A first application of the described computer model to atrial fibrillation can be found in [33].

Acknowledgment

This study was supported by the Austrian Science Fund (FWF) under grant P16759-N04. The authors would like to thank V. Jacquemet for useful comments on the theoretical background.

References

- Nattel S. New ideas about atrial fibrillation 50 years on. *Nature* 2002; 415: 219-226.
- Schilling RJ. Which Patient Should Be Referred to an Electrophysiologist: Supraventricular Tachycardia. *Heart* 2002; 87: 299-304.
- Wijffels MC, Kirchhof CJ, Dorland R, Allesie MA. Atrial Fibrillation Begets Atrial Fibrillation: A Study in Awake Chronically Instrumented Goats. *Circulation* 1995; 92: 1954-1968.
- Allesie M, Ausma J, Schotten U. Electrical, contractile and structural remodeling during atrial fibrillation. *Cardiovasc Res* 2002; 54: 230-246.
- Wieser L, Fischer G, Hintringer F, Ho SY, Tilg B. Reentry Anchoring at a Pair of Pulmonary Vein Ostia. *LNCS* 2005; 3504: 183-194.
- Vigmond EJ, Ruckdeschel R, Trayanova N. Reentry in a Morphologically Realistic Atrial Model. *J Cardiovasc Electrophysiol* 2001; 12: 1046-1054.
- Virag N, Jacquemet V, Henriquez CS, Zozor S, Blanc O, Vesin JM, et al. Study of atrial arrhythmias in a computer model based on magnetic resonance images of human atria. *Chaos* 2002; 12: 754-763.
- Siregar P, Julen N, Sinteff JP. Computational Integrative Physiology: At the Convergence of the Life and Computational Sciences. *Methods Inf Med* 2003; 42: 177-184.
- Harrild DM, Henriquez CS. A Computer Model of Normal Conduction in the Human Atria. *Circ Res* 2000; 87: e25-e36.
- Vigmond EJ, Aguel F, Trayanova NA. Computational Techniques for Solving the Bidomain Equations in Three Dimensions. *IEEE Trans Biomed Eng* 2002; 49: 1260-1269.
- Zozor S, Blanc O, Jacquemet V, Virag N, Vesin JM, Pruvot E, et al. A Numerical Scheme for Modeling Wavefront Propagation on a Monolayer of Arbitrary Geometry. *IEEE Trans Biomed Eng* 2003; 50: 412-420.
- Potse M, Dubé B, Richer J, Vinet A, Gulrajani RM. A comparison of monodomain and bidomain reaction-diffusion models for action potential propagation in the human heart. *IEEE Trans Biomed Eng* 2006; 53: 2425-2435.
- Blanc O, Virag N, Vesin JM, Kappenberger L. A Computer Model of Human Atria with Reasonable Computation Load and Realistic Anatomical Properties. *IEEE Trans Biomed Eng* 2001; 48: 1229-1237.
- Seeger M, Fischer G, Modre R, Messnarz B, Hanser F, Tilg B. Lead field computation for the electrocardiographic inverse problem – finite elements versus boundary elements. *Comput Methods Programs Biomed* 2005; 77: 241-252.
- Ramirez RJ, Nattel S, Courtemanche M. Mathematical analysis of canine atrial action potentials: rate, regional factors, and electrical remodeling. *Am J Physiol* 2000; 279: H1767-H1785.
- Spach MS, Miller WTI, Barr RC, Geselowitz DB. Electrophysiology of the internodal pathways? In: Little R, editor. *Physiology of Atrial Pacemakers and Conductive Tissue*. Armonk, NY: Futura Publishing Co; 1980. pp 367-380.
- Ho SY, Sanchez-Quintana D, Anderson RH. Can anatomy define electric pathways? In: *International Workshop on Computer Simulation and Experimental Assessment of Electrical Cardiac Function*; 1998. pp 77-86.
- Kucera JP, Kléber AG, Rohr S. Slow Conduction in Cardiac Tissue, II – Effects of Branching Tissue Geometry. *Circ Res* 1998; 83: 795-805.
- Tilg B, Fischer G, Modre R, Hanser F, Messnarz B, Schocke M, et al. Model-Based Imaging of Cardiac Electrical Excitation in Humans. *IEEE Trans Med Imaging* 2002; 21: 1031-1039.
- Pfeifer B, Hanser F, Seeger M, Hintermüller C, Modre-Osprian R, Fischer G, et al. Modeling using Active Appearance Models and Morphological Operators. *Proc SPIE, Medical Imaging 2005: Visualization, Image-Guided Procedures, and Display*; 2005. pp 5744-5732.
- Ho SY, Sanchez-Quintana D, Cabrera JA, Anderson RH. Anatomy of the Left Atrium: Implications for Radiofrequency Ablation of Atrial Fibrillation. *J Cardiovasc Electrophysiol* 1999; 10: 1525-1533.
- Roithinger FX, Cheng J, Sippens-Groenewegen A, Lee RJ, Saxon LA, Scheinman MM, et al. Use of Electroanatomic Mapping to Delineate Transseptal Atrial Conduction in Humans. *Circulation* 1999; 100: 1791-1797.
- Seemann G, Höper C, Sachse FB, Dössel O, Holden AV, Zhang H. Heterogeneous three-dimensional anatomical and electrophysiological model of human atria. *Phil Trans R Soc* 2006; 364: 1464-1481.
- Gozolits S, Fischer G, Berger T, Hanser F, Abou-Harb M, Tilg B, et al. Global P Wave Duration on the 65-Lead ECG: Single-Site and Dual-Site Pacing in the Structurally Normal Human Atrium. *J Cardiovasc Electrophysiol* 2002; 13: 1240-1245.
- Plank G, Leon LJ, Kimber S, Vigmond EJ. Defibrillation Depends on Conductivity Fluctuations and the Degree of Disorganization in Reentry Patterns. *J Cardiovasc Electrophysiol* 2005; 16: 205-216.
- Fischer G, Pfeifer B, Seeger M, Hintermüller C, Hanser F, Modre R, et al. Computationally efficient noninvasive cardiac activation time imaging. *Methods Inf Med* 2005; 44: 674-686.
- Jacquemet V, Henriquez CS. Finite volume stiffness matrix for solving anisotropic cardiac propagation in 2-D and 3-D unstructured meshes. *IEEE Trans Biomed Eng* 2005; 52: 1490-1492.

28. Fast VG, Kléber AG. Cardiac tissue geometry as a determinant of unidirectional conduction block: assessment of microscopic excitation spread by optical mapping in patterned cell cultures and in a computer model. *Cardiovasc Res* 1995; 29: 697-707.
29. Jalife J, Berenfeld O, Mansour M. Mother rotors and fibrillatory conduction: a mechanism of atrial fibrillation. *Cardiovasc Res* 2002; 54: 204–216.
30. Wieser L, Fischer G, Nowak CN, Tilg B. Fibrillatory Conduction in Branching Atrial Tissue – Insight from Volumetric and Monolayer Computer Models. *Comput Methods Programs Biomed. Comput Methods Programs Biomed* 2007; 86: 103-111.
31. Chauvin M, Shah DC, Haïssaguerre M, Marcellin L, Brechenmacher C. The Anatomic Basis of Connections Between the Coronary Sinus Musculature and the Left Atrium in Humans. *Circulation* 2000; 101: 647-652.
32. de Ponti R, Ho SY, Salerno-Uriarte JA, Tritto M, Spadacini G. Electroanatomic Analysis of Sinus Impulse Propagation in Normal Human Atria. *J Cardiovasc Electrophysiol* 2002; 13: 1-10.
33. Rantner LJ, Wieser L, Stühlinger MC, Hintringer F, Tilg B, Fischer G. Detection of Phase Singularities in Triangular Meshes. *Methods Inf Med* 2007; 46: 646-654.

Correspondence to:

Leonhard Wieser
University for Health Sciences, Medical Informatics and
Technology (UMIT)
Eduard-Wallnöfer-Zentrum 1/G3
6060 Hall in Tirol
Austria
E-mail: leonhard.wieser@umit.at